TU Delft

Delft University of Technology

Kinetic Control of Morphology and Composition in Ge/GeSn Core/Shell Nanowires

Assali, Simone; Bergamaschini, Roberto; Scalise, Emilio; Verheijen, Marcel A.; Albani, Marco; Dijkstra, Alain; Li, Ang; Koelling, Sebastian; Bakkers, Erik P.A.M.; More Authors

DOI
10.1021/acsnano.9b09929

Publication date
2020

Document Version
Final published version

Published in
ACS Nano

Citation (APA)
Assali, S., Bergamaschini, R., Scalise, E., Verheijen, M. A., Albani, M., Dijkstra, A., Li, A., Koelling, S., Bakkers, E. P. A. M., & More Authors (2020). Kinetic Control of Morphology and Composition in Ge/GeSn Core/Shell Nanowires. *ACS Nano*, *14*(2), 2445-2455. https://doi.org/10.1021/acsnano.9b09929

Important note
To cite this publication, please use the final published version (if applicable).
Please check the document version above.

Copyright
Other than for strictly personal use, it is not permitted to download, forward or distribute the text or part of it, without the consent of the author(s) and/or copyright holder(s), unless the work is under an open content license such as Creative Commons.

Takedown policy
Please contact us and provide details if you believe this document breaches copyrights.
We will remove access to the work immediately and investigate your claim.

This work is downloaded from Delft University of Technology.
For technical reasons the number of authors shown on this cover page is limited to a maximum of 10.

ACS NANO

www.acsnano.org

ARTICLE

Kinetic Control of Morphology and Composition in Ge/GeSn Core/Shell Nanowires

Simone Assali,*,¶ Roberto Bergamaschini,*,¶ Emilio Scalise,*,¶ Marcel A. Verheijen, Marco Albani, Alain Dijkstra, Ang Li, Sebastian Koelling, Erik P. A. M. Bakkers, Francesco Montalenti, and Leo Miglio

Cite This: ACS Nano 2020, 14, 2445−2455

Read Online

ACCESS | Metrics & More | Article Recommendations | Supporting Information

ABSTRACT: **The growth of Sn-rich group-IV semiconductors at the nanoscale can enrich the understanding of the fundamental properties of metastable GeSn alloys. Here, we demonstrate the effect of the growth conditions on the morphology and composition of Ge/GeSn core/shell nanowires by correlating the experimental observations with a theoretical interpretation based on a multiscale approach. We show that the cross-sectional morphology of Ge/GeSn core/shell nanowires changes from hexagonal to dodecagonal upon increasing the supply of the Sn precursor. This transformation strongly influences the Sn distribution as a higher Sn content is measured under the {112} growth front. *Ab initio* DFT calculations provide an atomic-scale explanation by showing that Sn incorporation is favored at the {112} surfaces, where the Ge bonds are tensile-strained. A phase-field continuum model was developed to reproduce the morphological transformation and the Sn distribution within the wire, shedding light on the complex growth mechanism and unveiling the relation between segregation and faceting. The tunability of the photoluminescence emission with the change in composition and morphology of the GeSn shell highlights the potential of the core/shell nanowire system for optoelectronic devices operating at mid-infrared wavelengths.**

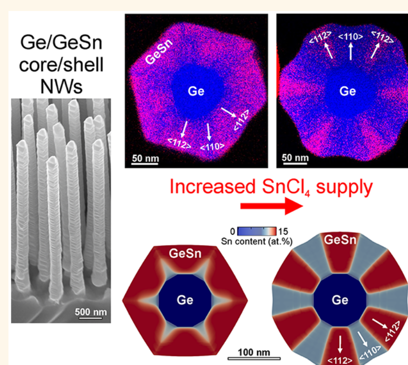

KEYWORDS: *semiconductor nanowire, germanium tin, heterostructure, segregation, kinetic growth model, first-principles calculations, photoluminescence*

Downloaded via TU DELFT on March 19, 2020 at 11:28:35 (UTC).
See https://pubs.acs.org/sharingguidelines for options on how to legitimately share published articles.

Direct band gap germanium−tin (GeSn) alloys are at the forefront in the development of optoelectronic devices operating at mid-infrared wavelengths and are fabricated on a silicon platform.[1] The epitaxial growth of GeSn layers is commonly performed on a Ge/Si virtual substrate (Ge-VS), and it provides full integration with the current Si-technology manufacturing processes.[2−5] However, as the lattice mismatch between GeSn and Ge increases with Sn content, the compressive strain in the GeSn layer shifts upward the compositional threshold for achieving a direct band gap in Sn-rich GeSn semiconductors.[6] In addition, the residual strain in the growing GeSn layer, after plastic relaxation, reduces the incorporation of Sn, eventually leading to segregation and phase separation, with the formation of Sn droplets at the surface.[4,7,8] This effect is especially pronounced when GeSn is grown directly on a Si substrate, where the lattice mismatch can reach values above 4%.[9] Enhanced strain relaxation can be achieved in a one-dimensional geometry, using semiconductor nanowires (NWs) grown from a metal catalyst by the vapor−liquid−solid (VLS) method. This configuration was recently exploited to fabricate axial and radial GeSn-based NW heterostructures, reaching incorporation of Sn well above the 9 at. % threshold required to achieve a (strain-free) direct band semiconductor.[6,10−13] The use of pure Sn catalysts resulted in the growth of GeSn NWs with compositions up to 19 at. % and optical emission at mid-infrared wavelengths.[14] In addition, by controlling the segregation of Sn droplets on the NW sidewall, the growth of Sn-seeded $Ge_{0.92}Sn_{0.08}$ branches on $Ge_{0.96}Sn_{0.04}$ trunks was demonstrated.[15] When moving to a Ge/GeSn core/shell NW geometry, the lattice mismatch is partially accommodated by transferring some strain into the Ge core, thus promoting strain relaxation in the GeSn shell without the nucleation of extended defects.[12,16,17] When the NW core diameter is smaller than the shell thickness, the core behaves as a compliant substrate, accommodating the lattice mismatch of

Received: December 17, 2019
Accepted: January 23, 2020
Published: January 23, 2020

© 2020 American Chemical Society

https://dx.doi.org/10.1021/acsnano.9b09929
ACS Nano 2020, 14, 2445−2455

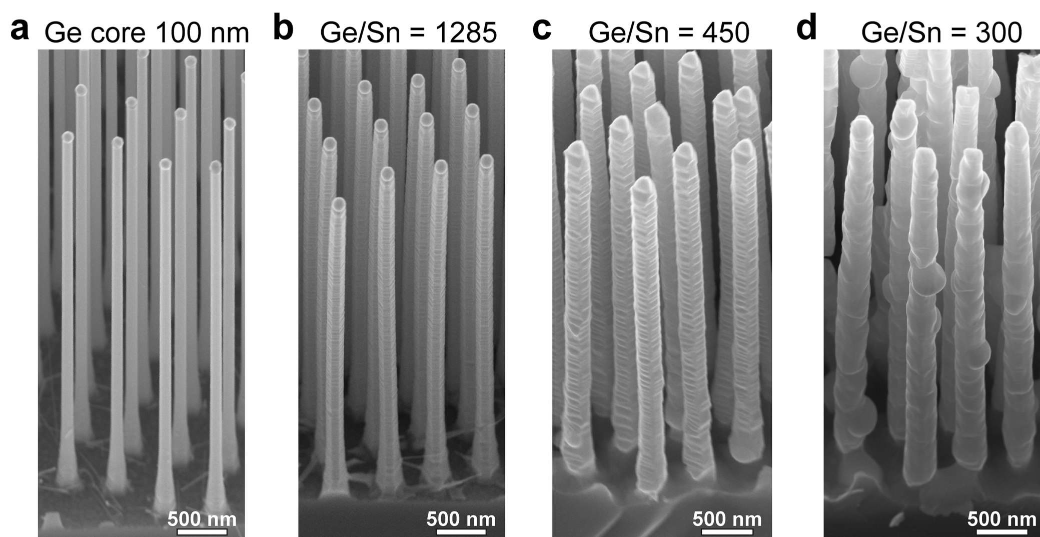

Figure 1. (a−d) SEM images of the Ge/GeSn core/shell NW arrays (tilting angle 30°) grown using a Ge core diameter of 100 nm (a) and a GeSn shell with a Ge/Sn ratio of 1285 (b), 450 (c), and 300 (d).

the system without bending.[18,19] Moreover, the incorporation of Sn in Ge increases as the compressive strain is progressively relieved with increasing shell thickness, by a mechanism of compositional pulling during the shell growth.[16] However, at larger core diameters the shell will experience higher strain, eventually inducing plastic deformation with the nucleation of defects and surface roughening.[17]

In this work, we show how the morphology and composition of a GeSn shell grown on a Ge core NW are strongly dependent on the growth conditions. At a higher supply of the tin tetrachloride ($SnCl_4$) precursor, the symmetry of the NW cross-section changes by the evolution of the corners in between the {112} facets into {110} facets. At the same time, enhanced segregation is observed, with an increasing difference in composition between Sn-poor ⟨110⟩-oriented stripes and Sn-rich {112} facets. In addition, at the highest supply of the Sn precursor, phase separation occurs and multiple Sn droplets are visible on the NW sidewall. The experimental observations are then rationalized theoretically by a multiscale approach. First, the shape transition will be interpreted by a continuum kinetic growth model, including surface diffusion. Then, first-principles calculations will be exploited to assess the origin of the different compositions within the facets and to extend the growth model in order to simultaneously trace the evolution of shape and composition. The agreement between experiments and theory highlights the strong correlation between faceting and segregation dynamics in the Ge/GeSn core/shell NW system.

RESULTS AND DISCUSSION

Epitaxial Growth. Arrays of ⟨111⟩-oriented Ge/GeSn core/shell NWs were grown on a Ge(111) wafer in a chemical vapor deposition (CVD) reactor using the VLS-growth method and nanoimprint-patterned gold islands as a catalyst.[12,16,17] The untapered growth of the 100 nm Ge core NWs was performed at 320 °C using monogermane (GeH_4) precursor, followed by the GeSn shell growth at 300 °C with the additional supply of tin tetrachloride ($SnCl_4$) and hydrogen chloride (HCl) precursors. The effect of the $SnCl_4$ precursor flow on the morphology of the GeSn shell is shown in Figure 1. A fixed growth time of 2 h was used in combination with a Ge/Sn ratio in the gas phase ranging from 1285 to 300. We note that when the $SnCl_4$ precursor is introduced in the CVD reactor, the axial NW growth is suppressed, while the radial GeSn shell growth is promoted.[12,17] An increase in the diameter of the core/shell NWs is visible with increasing (decreasing) supply of the $SnCl_4$ precursor (Ge/Sn ratio), as visible in Figure 1b−d. For Ge/Sn = 1285 a more complex faceting of the GeSn shell morphology is observed (Figure 1b), which becomes more prominent at a lower Ge/Sn ratio of 450 (Figure 1c). Interestingly, when the $SnCl_4$ precursor flow is increased further (Ge/Sn = 300), large Sn droplets are observed on the NW sidewall (Figure 1d), as discussed in more detail later in the text. The $SnCl_4$ flow is not only a crucial parameter to control the thickness of the GeSn shell but also has a strong effect on the segregation of Sn and, in turn, on the NW morphology. A detailed insight into the evolution of the thickness and morphology of the GeSn shell is obtained using energy-dispersive X-ray spectroscopy (EDX) compositional maps acquired in cross-sectional scanning-TEM (STEM) (Figure 2). In the Ge/Sn = 1285 sample (Figure 2a) a 20−30 nm thick GeSn shell terminated by six wide {112} facets connected by small rounded corners, possibly corresponding to six {110} nanofacets, is visible around the 100 nm Ge core. The EDX line scans acquired along the radial ⟨112⟩ and ⟨110⟩ directions are shown in Figure 2b, with a Sn content of ~8 at. % that is estimated on the main {112} facets. In addition, Sn-poor triangular regions (~4 at. %) are observed along ⟨110⟩, which are likely related to initial {110} facets inherited from the shape of the Ge core (see below), which disappear during the shell growth. When the $SnCl_4$ flow is increased (Ge/Sn = 450), a thicker 65 ± 5 nm shell with Sn content up to 12−13 at. % along the radial ⟨112⟩ directions and 7−10 at. % along the radial ⟨110⟩ directions is obtained (Figure 2c,d). Sn-poor triangular regions along ⟨110⟩ extend into the inner part of the shell, narrowing down to a sunburst-like geometry, similar to what is observed when using a 50 nm Ge core.[12,16] However, a more inhomogeneous morphology of the cross-section of the NWs is present when growing on 100 nm Ge cores, which is induced by the increased strain in the NWs[17] and by the higher $SnCl_4$ supply in the gas phase.

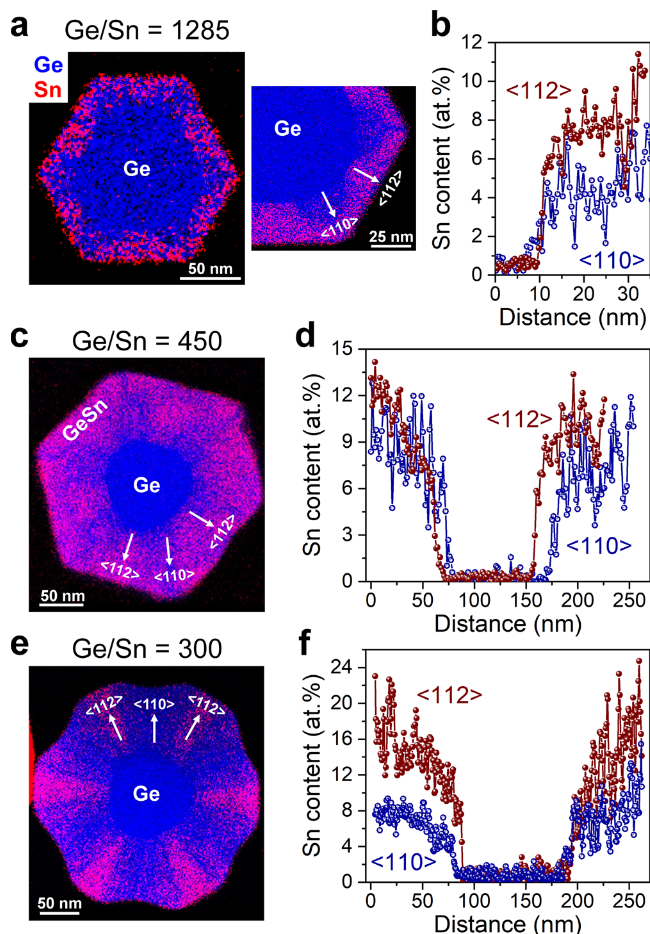

Figure 2. (a−f) Cross-sectional EDX compositional maps and related line-profiles along the ⟨112⟩ and ⟨110⟩ radial directions of the NWs, acquired for Ge/Sn ratios of 1285 (a, b), 450 (c, d), and 300 (e, f). Enhanced Sn incorporation along the ⟨112⟩ radial direction of the GeSn shell is observed with increasing $SnCl_4$ supply.

Indeed, an even larger change in the morphology of the GeSn shell is observed at the highest $SnCl_4$ flow (Ge/Sn = 300), where enhanced segregation of Sn leads to phase separation with the formation of Sn droplets at multiple positions along the sidewall (Figure 1d). The cross-sectional EDX map in Figure 2e was acquired on a segment of the NW without Sn droplets. A 12-fold shape of the cross-section is observed with alternating Sn-rich and Sn-poor regions. As indicated in Figure 2f, the Sn content increases from 8 at. % up to 18 at. % along the ⟨112⟩ direction, while a lower Sn content of 5−9 at. % is observed along the ⟨110⟩ direction.

The plot of the radial growth rate estimated along the ⟨110⟩ and ⟨112⟩ directions of the GeSn shell as a function of the Ge/Sn precursor supply is shown in Figure 3. Two different data sets for 100 nm (from Figure 2) and 50 nm Ge cores (refs 12, 16) are plotted. At a fixed GeH_4 flow, the GeSn radial growth rate increases with the $SnCl_4$ flow, and it becomes 4× times faster when moving from the low-Sn case at Ge/Sn = 1285 to the richest one at Ge/Sn = 300 grown on the 100 nm Ge cores, which indicates that vapor−solid growth occurs in a Sn-limited regime. The same trend is observed when using 50 nm cores. In addition, for a Ge/Sn ratio in the 450−550 range a higher growth rate is obtained around 50 nm cores compared to 100 nm cores, which most likely results from the reduced

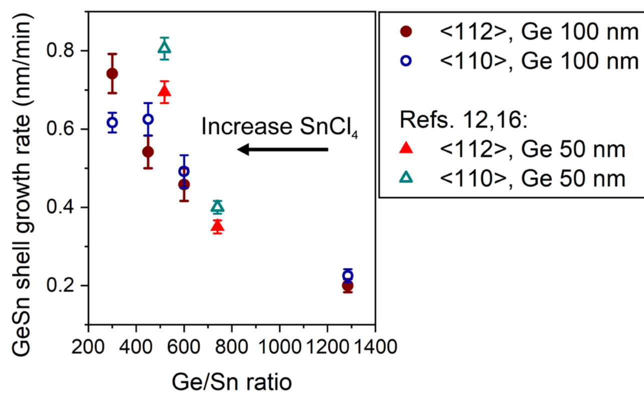

Figure 3. Plot of the growth rate of the GeSn shell as a function of the Ge/Sn ratio, estimated from Figure 2 (solid and hollow circles). The data points adapted from refs 12 and 16 are also shown (solid and hollow triangles).

amount of strain in the shell during growth around the thinner Ge NWs. We highlight that the increased GeSn growth rate with the $SnCl_4$ precursor flow is similar to what is observed in conventional planar GeSn growths, where the growth kinetics are controlled by the $SnCl_4$ supply and the growth temperature, thus suggesting a co-decomposition mechanism with the GeH_4 precursor.[20,21] Interestingly, in the case of Ge/Sn = 300, the growth rate along the ⟨112⟩ direction is ∼20% faster than along the ⟨110⟩ direction, resulting in the dodecagonal shape. The transition from a 6-fold to a 12-fold symmetry of the NW cross-section will be explained below in terms of the increased shell growth rate.

The increased amount of Sn supplied during the GeSn shell growth not only affects the growth rates but also increases the number of Sn droplets on the NW sidewall, as highlighted in the STEM image in Figure 4a of a NW grown using a Ge/Sn = 300. The associated EDX maps in Figure 4b,c show the presence of Sn-rich droplets located not only on the shell surface but also inside in the GeSn shell. Cross-sectional EDX (Figure 4d) measurements performed on a portion of the NW with a droplet shows a Sn content of ∼99.7 at. % Sn in the droplet, with the remaining ∼0.3 at. % Ge signal being at the resolution limit of the EDX analysis. In addition, the same orientation-dependent Sn incorporation is observed in the shell as in Figure 2e, but a depletion of Sn in the outer 20−40 nm of the GeSn shell is visible in Figure 4d (dashed line region). Thus, when the Sn droplet forms on the sidewall, the shell growth continues and Sn atoms diffuse to the droplet rather than being incorporated in the growing GeSn shell. Furthermore, the presence of the Sn droplets does not compromise the metastable state of the GeSn shell,[12] since the bulk diffusion of Sn atoms from the inner portion of the shell toward the surface is negligible.[8,9,11,22,23] As a result, the Sn segregation on the NW sidewall seems to have a less severe effect on the structural quality of the NW samples when compared to planar GeSn growth, where the presence of liquid Sn-rich droplets (above the Ge−Sn eutectic temperature of 231 °C) induces phase separation of the strained GeSn layer underneath.[24] The cross-sectional TEM and corresponding fast-Fourier transform (FFT) images for the shell and droplet regions are shown in Figure 4e, which indicate the presence of the β-Sn phase.[25]

Theoretical Growth Model. We first focus on the modeling of the shape transition from the dodecagonal

https://dx.doi.org/10.1021/acsnano.9b09929
ACS Nano 2020, 14, 2445−2455

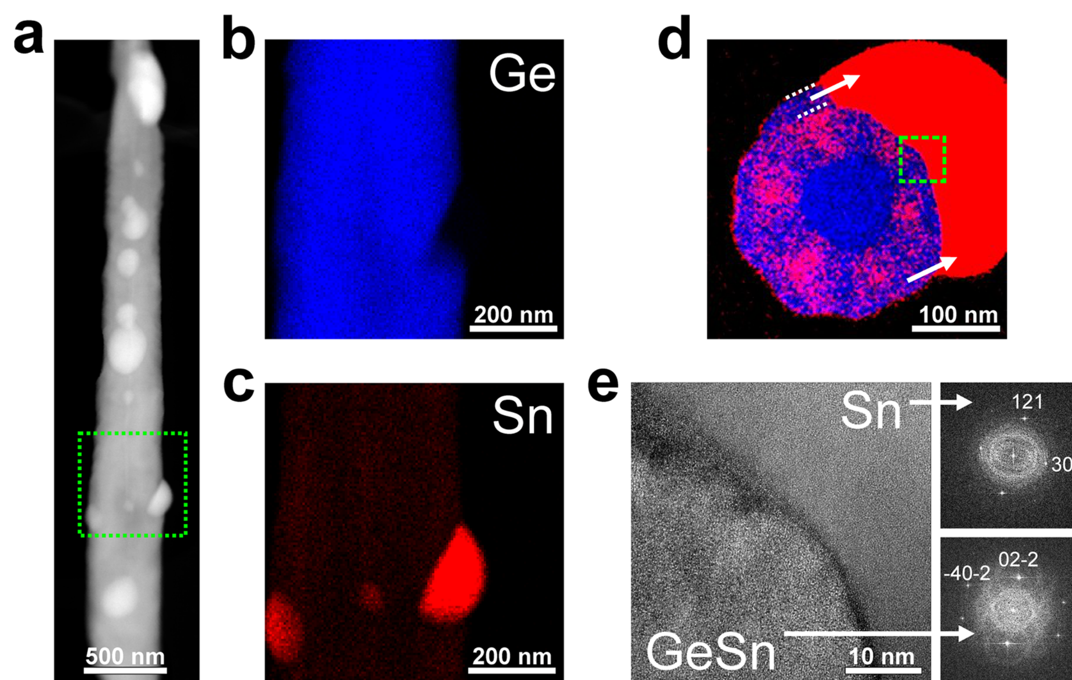

Figure 4. (a) STEM image of a NW grown with Ge/Sn = 300. (b, c) EDX compositional maps for Ge (b) and Sn (c) atoms showing phase separation with the presence of Sn droplets on the NW sidewall. (d) Cross-sectional EDX compositional map acquired on a spot where a Sn droplet is present. (e) Bright-field TEM image of the GeSn−Sn droplet interface acquired along the [$\bar{1}$22] zone axis, tilted 15° from the main ⟨111⟩ axis to visualize lattice fringes in the Sn particle. Insets: Corresponding FFT images of the Sn droplet and GeSn shell regions.

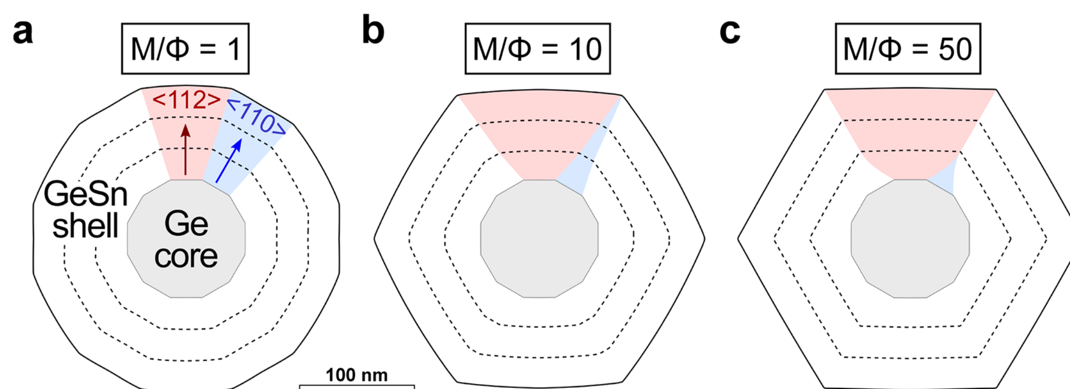

Figure 5. (a−c) Profile evolution from simulations with isotropic deposition and faster adatom incorporation along the ⟨110⟩ direction, as a function of the mobility/growth rate ratio M/Φ of 1 (a), 10 (b), and 50 (c). A regular dodecagon is set as initial profile, mimicking the Ge core shape, and profiles are reported at three subsequent times. Colored sectors are shown to view the progressive evolution of the two facets along the ⟨112⟩ (red) and ⟨110⟩ (blue) directions.

cross-section observed at low Ge/Sn ratio (Figure 2e) to the hexagonal one at high Ge/Sn ratio (Figure 2a,c). Since the Ge cores expose six {112} and six {110} facets with similar lateral extension,[17] any change in the shell morphology occurring during the growth of the GeSn shell stems from the competition between the ⟨112⟩ and the ⟨110⟩ growth fronts. In the following description, limited to the two-dimensional (111)-cross-section of the NW, such growth fronts will be modeled as {112} and {110} facets even if they can in principle result from a combination of different facets, especially in the case of low Ge/Sn ratio. In a minimal model, we consider the GeSn growth process as resulting from the combined effect of deposition from the precursors in the gaseous phase and redistribution of adatoms by surface diffusion. An isotropic distribution of the incoming material is assumed. The movements of adatoms formed at the surface follow the local chemical potential μ. Diffusion is effective over a distance of the order of the diffusion length λ, and it is determined by the square root of the ratio between the mobility M and the growth rate Φ, *i.e.*, $\lambda \sim \sqrt{M/\Phi}$. As the experiments show a significant variation in the growth rate as a function of the Ge/Sn ratio (Figure 3), material redistribution is expected to play a key role in the formation of the 6-fold symmetric shell. The shape transition can then be rationalized by considering diffusion from {112} to {110} facets, as a consequence of a lower μ on the {110} facets than on the {112} ones. Such a significant difference is not justifiable by energetic arguments. Surface energies of {112} and {110} for pure Ge are indeed almost identical[26] (Supporting Information S1), and they are not expected to change significantly, particularly during the first stages of growth where the Sn content is low. Since the Sn incorporation in the shell is well

https://dx.doi.org/10.1021/acsnano.9b09929
ACS Nano 2020, 14, 2445−2455

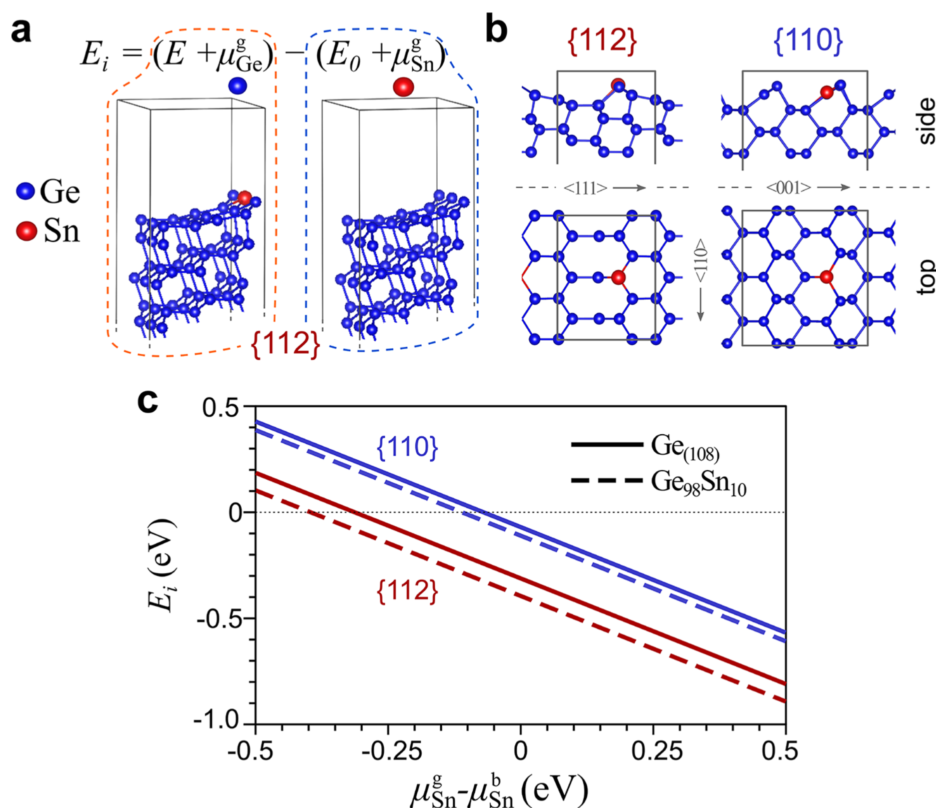

Figure 6. (a) Representation of the simulation cell used for the *ab initio* calculation of the incorporation energy for a {112} surface, comparing the state with or without a Sn surface atom. (b) Lateral and top views of the atomic structure of the {112} and {110} surfaces. A Sn atom (red) is positioned at the most favorable site. The unit cell is marked by a dashed rectangle. (c) Incorporation energy computed by *ab initio* calculations of both {112} and {110} facets as a function of the Sn chemical potential.

above the ∼1 at. % equilibrium solubility limit in Ge, the growth kinetics play a crucial role in the out-of-equilibrium GeSn deposition. However, an accurate characterization of the dynamics of Sn incorporation at the microscopic level would be extremely complex, requiring a detailed analysis of many atomistic processes, including the variety of chemical reactions involving the gaseous precursors. Nonetheless, the combined effect of these processes can be condensed into an effective parameter, the adatom incorporation lifetime τ, accounting for the net rate of adatom incorporation on the different facets. As discussed in refs 27 and 28, a growth model including the incorporation kinetics can be set up by considering $\mu = \mu_{eq} + \tau v$. $\mu_{eq} \sim \kappa\gamma$ is the thermodynamic contribution to the adatom chemical potential, here assumed proportional to the local curvature κ with isotropic surface energy density γ, and strain is neglected. v is the profile velocity itself and is determined by deposition and surface diffusion: $v = \Phi + \nabla_S\cdot[M\nabla_S\mu]$. τ can be defined as a continuum function of the surface orientation,[28,29] with local maxima in correspondence with the observed facets. Indeed, in a kinetic growth regime, the (convex) crystal shape consists of those facets growing at a slower rate (*i.e.*, high τ).[30] For the present 2D case study, 12 local maxima (one every 30°) are imposed, corresponding to the set of ⟨112⟩ and ⟨110⟩ directions in the (111)-cross-sectional plane of the NW. Following the previous considerations on the shape transition, τ maxima in the ⟨112⟩ directions are set greater than those along the ⟨110⟩ ones. A factor of ∼2 is estimated (*a posteriori*) to return a satisfactory match between simulation results and experiments (see below). A computationally efficient phase-field model is exploited to implement the evolution equations (see Methods section for details).

Figure 5 reports sequences of profile evolution obtained by simulations for three different ratios of mobility over growth rate (M/Φ = 1, 10, 50) starting from a 100 nm dodecagonal Ge core. If deposition is fast enough to frustrate interfacet diffusion (Figure 5a), a dodecagonal faceted shape, formed by both {112} and {110} facets, is obtained as adatoms distribute over a short range, which is only sufficient to keep the facets straight as corresponding to local maxima in τ. Then, by increasing the M/Φ ratio (*i.e.*, the diffusion length λ) the material exchange between the {112} and {110} facets is enabled and the slowest growing {112} facets (long τ) prevail over the {110}, converting the initial dodecagonal shape imposed by the core into one hexagon (Figure 5b,c). Since the shape transition occurs by diffusive dynamics, it requires a finite time to complete depending on the relative adatom mobility M/Φ, as evident by the different evolution paths of the central and right cases of Figure 5.

So far, we showed how the shape transition in the GeSn shell can be explained by considering different adatom incorporation kinetics on the two facets, without distinguishing between Ge and Sn atoms. However, experiments show that the morphological evolution occurs in combination with a nonuniform Sn distribution, consisting of a net enhancement of Sn content at the ⟨112⟩ growth fronts with respect to the ⟨110⟩ ones (Figure 2). In order to understand the origin of this difference in Sn incorporation, we compute the energy variation resulting by the exchange of Ge atoms at the shell surface with Sn atoms from the gas. The change in the total

https://dx.doi.org/10.1021/acsnano.9b09929
ACS Nano 2020, 14, 2445−2455

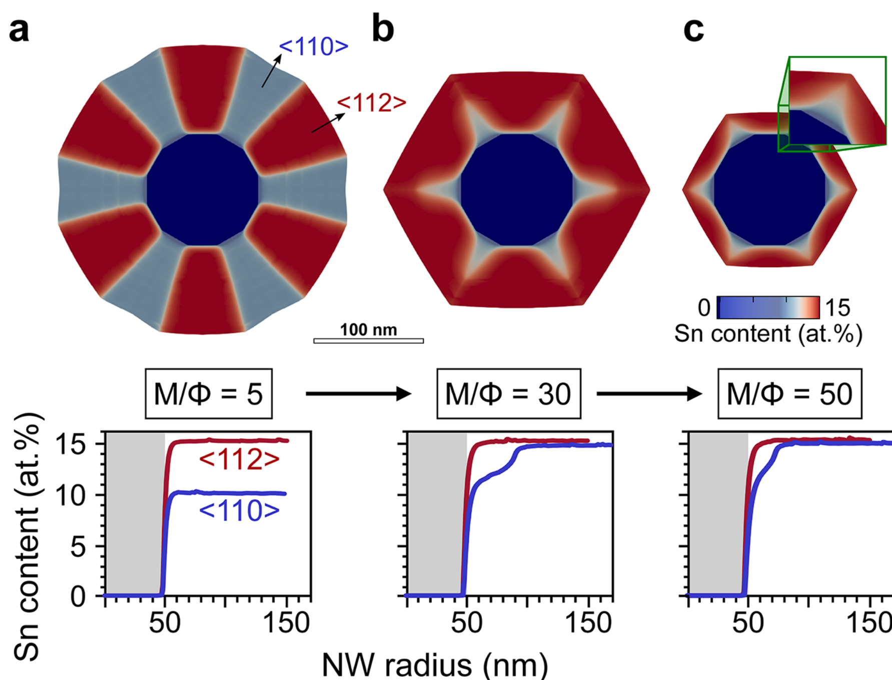

Figure 7. (a, b) Profiles obtained by growth simulations performed for different mobility/growth rate conditions M/Φ of 5 (a), 30 (b), and 50 (c), mimicking the experimental cases in Figure 2. Shell thicknesses are set to match the experimental ones. A magnification of one shell corner is reported for the case of slow deposition (c) to highlight the fast consumption of the {110} facet. The radial variation of Sn along both ⟨112⟩ and ⟨110⟩ directions is simulated up to a shell thickness of 100 nm.

energy of the crystal is estimated by *ab initio* thermodynamics, based on the density functional theory (DFT). Crystal slabs are cut along both {112} and {110} planes for both pure-Ge and GeSn at 9 at. % Sn. The former, illustrated in Figure 6a, is considered as representative of the pristine growth stages, while the latter corresponds to a later stage where a few GeSn layers have already been deposited on the Ge core. One of the Ge atoms is then replaced by Sn, and the difference in energy with respect to the previous state, $E - E_0$, is calculated. The procedure is repeated for every nonequivalent Ge site in the cell in order to select the energetically most favorable one. For the sake of simplicity, the selection was restricted only to the topmost layer of both {112} and {110} slabs. The optimal configuration for both facets is reported in Figure 6b, while a site-dependent analysis can be found in the Supporting Information S2. As the exchange process involves Ge and Sn atoms in the gas phase, with energy μ^{g}_{Ge} and μ^{g}_{Sn}, respectively, in order to estimate the actual energy gain due to the Sn incorporation, the total variation of energy $E_i = (E + \mu^{g}_{Ge}) - (E_0 + \mu^{g}_{Sn})$ has to be considered, as sketched in Figure 6a. This causes the result to depend on the partial pressures of both components, namely, of their precursors, which are indeed tuned in the experiment. The plot in Figure 6c shows the variation in E_i as a function of μ^{g}_{Sn} with respect to its bulk μ^{b}_{Sn}, with the assumption of $\mu^{g}_{Ge} = \mu^{b}_{Ge}$ (see Methods section for details). As evident, the {112} facet is predicted to have the lowest incorporation energy for any growth condition for both pure-Ge and GeSn slabs. For obvious reasons, this preference, tested for the initial layers, holds true for the subsequent shell growth, even if a more complex faceting may occur, so that we conclude that Sn is introduced more easily into the {112} fronts than the {110} fronts. Microscopically, this could be explained by noting that Ge−Ge bonds on the {112} surface are very stretched with respect to the bulk, in contrast with the bonds on the {110} surface. Thus, the replacement of a Ge atom by a Sn one is more convenient on the {112} facets, since the Ge−Sn bond length is larger than a Ge−Ge bond (see Supporting Information S2). As a result, {112} facets will grow with a higher Sn content than {110} facets, in agreement with the EDX results on all samples (Figure 2).[17] The negative slope of $E_i(\mu^{g}_{Sn})$ also indicates that the incorporation of Sn becomes more favorable when considering Sn-rich growth conditions (*i.e.*, low Ge/Sn ratio). In the opposite case, when μ_{Sn} is decreased below the bulk value, the energy E_i becomes positive and Sn incorporation is not favored anymore. It is worth noticing that the present analysis just states the energy advantage of placing a Sn atom at the surface with respect to leaving it in the gaseous phase, without considering neither the reaction mechanism by which the process occurs nor the kinetic path for it. Moreover, the option of forming liquid Sn droplets as in the experiments at high Sn fluxes is not explicitly considered and would introduce an upper limit to μ_{Sn} with respect to the plotted range.

Let us finally combine the kinetic description of the shape transition and the atomistic explanation of the different Sn content along the ⟨112⟩ and ⟨110⟩ directions into a comprehensive model, tackling both the shape and composition evolution during the shell growth. To keep the description as simple as possible and limit the number of parameters, we start from the kinetic growth model employed for Figure 5 and extend it to explicitly cope with the two alloy components, *i.e.*, Ge and Sn. The overall model concept is reported in ref 29 and follows the seminal idea proposed by Tersoff in ref 31 of limiting intermixing effects to only within a few atomic layers from the free surface.[32] Deposition and diffusion take place at the surface for each component i (of relative composition c_i), i, *i.e.*, $v_i = \Phi_i + \nabla_S \cdot [c_i M \nabla_S \mu_i]$ (same mobility M is assumed), and their combination determines the advancing of the growth

https://dx.doi.org/10.1021/acsnano.9b09929
ACS Nano 2020, 14, 2445−2455

front ($v = \sum v_i$) as well as the change in the surface composition ($\partial c_i/\partial t = v_i - c_i v$). In the region underneath the surface the composition profile remains frozen-in, as bulk diffusion is suppressed. When neglecting mixing enthalpy, the chemical potential for each component will only include an additional term from configurational entropy, *i.e.*, $\mu_i = (\mu_{eq} + \tau v) + kT \ln c_i$, with k the Boltzmann constant and T the temperature. The model parameters are then set identical to those of Figure 5, but for the flux of Sn Φ_{Sn} onto the surface. This is modulated as a function of the local profile orientation to include, in an effective way, the preference of Sn to stay on {112} surfaces, as indicated by experiments and atomistic simulations. A simple sinusoidal variation is considered with maxima along the ⟨112⟩ directions and minima in the ⟨110⟩ ones, resulting in a realistic Sn content of ∼10 at. % on {110} facets and ∼15 at. %, respectively.

Including the compositional field into the aforementioned phase-field approach enables us to simultaneously trace the advancing of the shell growth front and the Sn segregation effects. As already discussed for the shape transition (Figure 5), also in this coupled dynamics, the key is the relative role of diffusion and deposition, *i.e.*, the mobility/growth rate ratio M/Φ. In Figure 7 (see also Figure S4), we show three simulated profiles obtained by varying the M/Φ ratio in order to match the EDX maps of Figure 2. The Sn content is mapped by colors, and its radial variation along both ⟨112⟩ and ⟨110⟩ directions is plotted. The correspondence between simulation and experiments is compelling, as most of the key features are reproduced. In particular, in the case of Figure 7a, where adatom redistribution is quite limited, we achieve a dodecagonal shape with ⟨112⟩-Sn-rich sectors and ⟨110⟩-Sn-poor ones. A slight concavity in the ⟨110⟩ direction is also distinguishable, as a trace of the frustrated diffusion from the {112} regions toward the {110} regions. In the case of long-range diffusion (center and right Figure 7b,c), the kinetically preferred hexagonal shape is obtained right after deposition of a thin dodecagonal shell. The progressive shrinkage of the {110} facets, originating from the Ge core, is well marked by a Sn-poor triangular region which extends up to a certain shell thickness determined by the M/Φ ratio. As indicated in the plot of the composition along the ⟨110⟩ radius, the Sn content within the {110} sector is not constant but increases with the shell thickness. This is explained by the arrival of material diffusing from the Sn-rich {112} regions into the {110} region (see Figure S4), mixing with the Sn-poor adatoms deposited on the smaller {110} area.

It is worth noting that in the present work the systematic analysis of shape and composition was focused on samples with 100 nm cores, quite large compared to the ones typically discussed in the literature.[12,13,16,33] This was essential in order to have dodecagonal shapes. Indeed, in all other samples with smaller core radius (down to 50 nm) only a {112}-bounded hexagonal cross-section was observed for all Ge/Sn ratios (unless irregular, defected shapes were obtained).[17] This is compatible with the model as the shape transition depends on the relative extent of diffusion length with respect to the facet dimension. By reducing the core size it is then reasonable to expect that the kinetic shape is accessible by lower M/Φ ratio than required for the larger cores considered here. An example of the influence of the core size on the final shape of the resulting NW is shown in Figure 8. Even if theoretically, a dodecagonal structure on the 50 nm core could still be

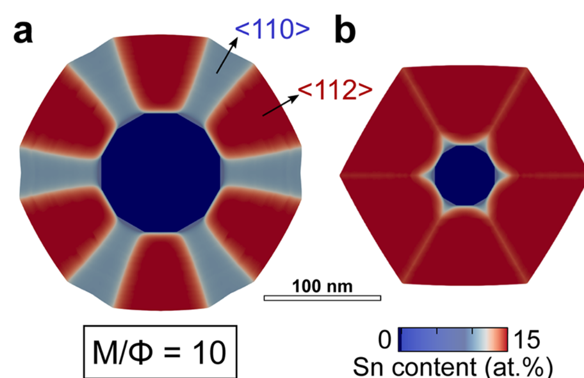

Figure 8. (a, b) Simulation profiles obtained for identical mobility/growth rate conditions (M/Φ = 10) and Ge core radius of 100 nm (a) and 50 nm (b).

obtained by lowering further M/Φ, the relevant growth regime may not have been explored in growth experiments yet.

In the present simulations the appearance of nanometer-thin, Sn-poor (1 at. % lower than facets) stripes is observed along the ⟨110⟩ directions. This resembles the sunburst-like structure commonly observed in nanowires. In order to achieve the localized Sn segregation observed in experiments (∼5% lower than facets), additional effects, *e.g.*, mobility differences between Ge and Sn adatoms, need to be included in the model.

Optical Properties. The effect of the incorporation and segregation of Sn on the optical properties of the NWs is shown using low-temperature (4 K) photoluminescence (PL) measurements.[12] No PL emission was observed in the Ge/Sn = 1285 sample, which is most likely due to the low Sn incorporation (∼8 at. %) in combination with the highly compressively strained nature and reduced volume (20−30 nm thick) of the $Ge_{0.92}Sn_{0.08}$ shell. To promote an indirect to direct band gap transition in unstrained GeSn, the incorporation of Sn should be higher than 8−9 at. %, which is not achieved in the Ge/Sn = 1285 sample. No optical emission was also detected in the Ge/Sn = 300 sample (Figure 4), thus demonstrating that the severe Sn segregation and phase separation compromise the quality of the heterostructured NWs. The PL spectra for the samples grown with Ge/Sn = 450−600 are shown in Figure 9a. In the Ge/Sn = 600 sample (dark red curve) a single PL peak is observed at 0.44 eV (*i.e.*, 2.8 μm wavelength) with a fwhm of ∼80 meV. By increasing the $SnCl_4$ flow to Ge/Sn = 450 (blue curve) the optical emission shifts to 0.41 eV (*i.e.*, 3.0 μm wavelength) with a fwhm of 60−70 meV. The red-shift of the PL peak with increasing $SnCl_4$ supply (*i.e.*, enhanced Sn incorporation) is in agreement with what was observed for Ge/GeSn core/shell NWs grown using a 50 nm core and Ge/Sn = 518−740 from ref 12, which are also plotted as a comparison in Figure 9a. The higher, nonuniform Sn content (18−20 at. %) in the shell grown around the 100 nm cores compared to the (∼13 at. %) 50 nm NWs reduces the energy of the emitted PL, in agreement with the recent studies on GeSn thin films and nanostructures.[2,5,14] However, the emission energy of GeSn is also influenced by the higher residual compressive strain in the shell when grown around the thicker 100 nm Ge cores,[17] which increases the band gap value, thus in the opposite direction compared to the shift induced by a higher Sn incorporation. In addition, lower intensity and a broader emission peak are obtained for the NWs grown using the 100

https://dx.doi.org/10.1021/acsnano.9b09929
ACS Nano 2020, 14, 2445−2455

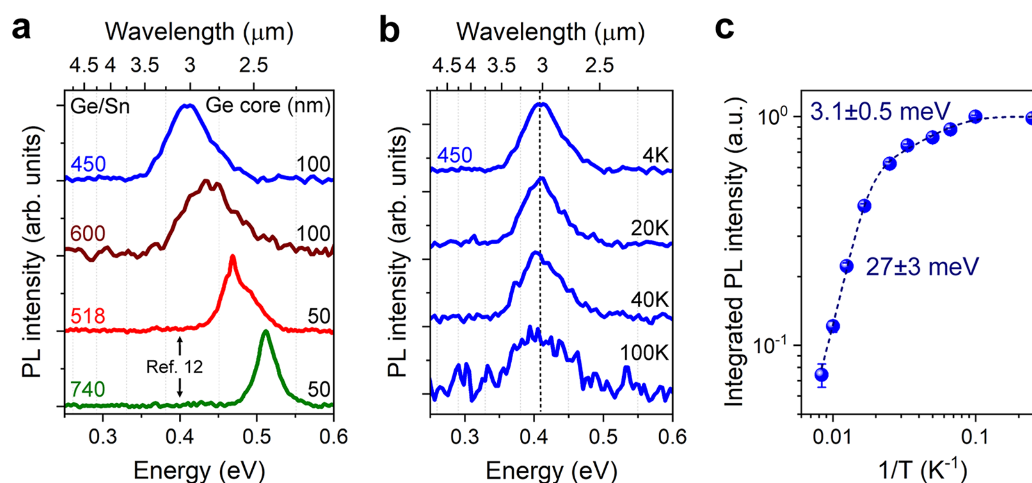

Figure 9. (a) PL spectra acquired at 4 K for Ge/GeSn core/shell NWs grown using a 100 nm core and a Ge/Sn ratio of 450 (blue curve) and 600 (dark red curve) measured at an excitation power density of 1.9 kW/cm^2 (976 nm laser). The data on Ge/GeSn core/shell NWs grown using a 50 nm core and a Ge/Sn ratio of 518 (red curve) and 740 (green curve) from ref 12 are also shown, measured at 7.8 W/cm^2 (405 nm laser). (b) PL spectra acquired in the 4−100 K temperature range for the sample grown with Ge/Sn = 450 and a Ge core of 100 nm. (c) Integrated PL intensity as a function of the inverse of the temperature for the data in (b).

nm Ge cores instead of 50 nm cores,[12] which would suggest reduced optical recombination in the presence of residual compressive strain and nonuniform Sn incorporation in the GeSn shell. We note that the PL emission at 4 K is most likely dominated by band-gap-related localized states, such as alloy fluctuations, impurities, or defects. To confirm this, PL measurements performed in the 4−100 K temperature range on the 100 nm Ge core and Ge/Sn = 450 shell sample (Figure 9b,c) show a quenching of the optical emission at ∼100 K. As a comparison, in the thinner 50 nm Ge core samples the PL emission is observed until 300 K, with a thermal detrapping from the localized states into the direct band gap emission above 100 K.[12] In Ge/GeSn core/shell NWs grown using a 100 nm Ge core the higher amount of compressive strain in the GeSn shell combined with the enhanced Sn segregation on the {112} facets of the shell leads to a rapid quenching of the PL emission with increasing temperature, thus indicating the limited optical properties of these core/shell NWs when compared to the ones grown using the 50 nm Ge core. Similarly, room-temperature PL emission was also promoted in strain-free GeSn NWs[14] and in GeSn thin films when underetched in free-standing microdisks.[34] Therefore, major care is required in minimizing strain and segregation in GeSn to enhance the optical properties at mid-infrared wavelengths while preserving room-temperature operation.

CONCLUSION

The growth of metastable GeSn semiconductors in a Ge/GeSn core/shell nanowire geometry has been investigated in-depth by combining experimental and theoretical analyses. We show that by increasing the supply of Sn atoms in the gas phase during growth, the morphology and composition of the GeSn shell is strongly affected. A 6-fold to 12-fold change in the symmetry of the NW cross-section by increasing the size of the six ⟨110⟩ corners in the GeSn shell with respect to the (main) six {112} facets is observed. Enhanced segregation of Sn is observed at higher Sn supply with an increasing compositional difference between the Sn-poor ⟨110⟩-oriented stripes and Sn-rich ⟨112⟩-oriented ones, eventually leading to phase separation and nucleation of Sn droplets on the NW sidewall.

In order to understand the GeSn growth mechanism at the nanoscale, a multiscale approach was exploited, and it reveals a deep connection between the Sn segregation effects and the morphological changes in the NW shell for different growth conditions. We predict that {110} facets (if present) incorporate a lower amount of Sn compared to {112} facets at any supply of Sn atoms in the gas phase during growth. Indeed, under the assumption that adatom incorporation on {112} facets is slower than on {110} facets our model reproduces the experimentally observed shapes and composition profiles with high accuracy. The interplay between facet-dependent incorporation and surface adatom kinetics is inferred to be the key process that determines both segregation of Sn and the morphology of the GeSn shell. Dedicated studies on the microscopic processes, especially on the complex surface chemistry processes of the GeSn precursors, will help to assess the origin of the kinetic effects. Interestingly, despite the simplifications made in our model, the developed 2D model provides an accurate description of the experimental findings, although it does not cover the whole complexity of the GeSn growth dynamics like misfit strain and plastic relaxation which might occur for large cores.[17] We conclude that these effects do not significantly affect the growth dynamics. In addition, we highlight the effect of strain and Sn segregation in reducing the optical emission of the GeSn shell when using a 100 nm Ge core compared to 50 nm. The 4 K photoluminescence emission in the thicker cores is dominated by localized states, with a quenching of the emission above 100 K, while in the thinner core band-to-band recombination is observed at room temperature. These findings clearly show that minimizing strain and segregation in the Ge/GeSn core/shell system is of paramount importance to preserve the high optical quality of these NWs at mid-infrared wavelengths.

METHODS

NW Growth and Characterization. The VLS growth of Au-catalyzed arrays of Ge/GeSn core/shell NWs was performed in a Aixtron CCS chemical vapor deposition reactor using H_2 as a carrier gas, following the growth protocol recently established in ref 12. Monogermane (GeH_4), tin tetrachloride ($SnCl_4$), and hydrogen

chloride (HCl) were used as precursors for the NW growth using H_2 as a carrier gas. The array of Au droplets with a diameter of 100 nm and a pitch of 500 nm was fabricated on a Ge(111) substrate using nanoimprint lithography. First, the nucleation of the Ge NWs was performed at 425 °C with the supply of the GeH_4 precursor and at a reactor pressure of 100 mbar. Next, the sample was cooled to 320 °C and the untapered Ge NWs were grown at a reactor pressure of 75 mbar. Lastly, the GeSn shell was grown at 300 °C for 2 h and at a reactor pressure of 50 mbar. The GeH_4 and HCl precursors were supplied with a constant molar fraction of 4×10^{-3} and 4×10^{-4}, respectively, while the $SnCl_4$ molar fraction was varied in the (3−10) $\times 10^{-6}$ range, leading to a Ge/Sn ratio in the gas phase of 1285−300.

Transmission electron microscopy (TEM) studies were performed using a probe-corrected JEOL ARM 200F, operated at 200 kV, equipped with a 100 mm^2 Centurio SDD EDS detector.

DFT. First-principles calculations are performed using DFT and a plane wave basis set as implemented in the Quantum Expresso code.[35] The exchange−correlation is treated in the generalized gradient approximation as parametrized by Perdew, Burke, and Ernzerhof, and projector-augmented wave pseudopotentials are used, setting a wave function cutoff of 60 Ry. The {110} and {112} Ge surfaces are modeled by using symmetric slabs with six atomic layers (108 atoms) and (3 × 2) and (3 × 1) in-plane periodicity, respectively, and considering their most stable reconstructions among different ones proposed in the literature.[36−39]

The incorporation energy of Sn onto the Ge surface is calculated as $E_i = (E + \mu^g_{Ge}) - (E_0 + \mu^g_{Sn})$, where E_0 is the DFT total energy of a pure Ge slab, while E is the energy of the corresponding lowest energy configuration with a Sn substituting a Ge atom on the surface. μ^g_{Ge} and μ^g_{Sn} are the chemical potential of Ge and Sn, respectively. The former is set to the chemical potential of bulk Ge, since it is expected that the conditions required to form a crystalline Ge shell should bring the interface close to the equilibrium with the underlying Ge core. In contrast, the chemical potential of Sn has been varied with respect to its bulk reference, in order to mimic changes of the Ge/Sn ratio. Thus, in Figure 6c the incorporation energy is plotted as a function of the variation of the Sn chemical potential with respect to its bulk value.

GeSn Shell Growth Model. The evolution of the GeSn NW shell during growth is investigated by a phase-field model coupling the kinetic description of the morphological evolution defined in ref 28 to the two component dynamics developed in ref 40 (see Supporting Information S3 for more details). The system is defined by two parameters: (i) the phase-field function φ, tracing implicitly the growth front as the diffuse-interface between the solid (where $\varphi = 1$) and the surrounding vacuum phase ($\varphi = 0$);[41] (ii) the composition field c specifying the local Sn content. The profile evolution then results from the net flux of both components at a given point: $\partial\varphi/\partial t = \sum_i(\Phi_i|\nabla\varphi| + \nabla\cdot[c_i M \nabla\mu_i])$, where Φ_i, c_i, and μ_i are the growth rate, the local composition, and the surface chemical potential of the ith (Sn or Ge) component. The mobility M is restricted at the surface region by setting $M(\varphi) \sim \varphi^2(1 - \varphi)^2$. At the same time, the imbalance in the flux of the two components is responsible for the eventual variation in the local composition c, as $\partial(c\varphi)/\partial t = \Phi_{Sn}|\nabla\varphi| + \nabla\cdot[cM\nabla\mu_{Sn}]$. While Ge deposition is set with a uniform rate Φ_{Ge} = 0.875 nm/s, the Sn growth rate varies as $\Phi_{Sn} = 0.125 + 0.025\cos(6\theta)$, with maxima corresponding to the ⟨112⟩ directions and minima in the ⟨110⟩ ones. The chemical potential of each component includes a (isotropic) surface energy and a kinetic term, undifferentiated for Sn and Ge for the sake of simplicity, and mixing entropy, *i.e.*, $\mu_i = \gamma[-\epsilon\nabla^2\varphi + (1/\epsilon)B'(\varphi)] + \epsilon\tau(\partial\varphi/\partial t) + kT\ln c_i$, with a double-well potential $B(\varphi) = (18/\epsilon)\varphi^2(1 - \varphi)^2$, where ϵ defines the width of the φ diffused interface for the phase-field description, k the Boltzmann constant, and T the temperature, here set equal to 320 °C in compliance with our experiments. The variation of incorporation times τ with respect to the profile orientation θ is obtained by the convenient formula of ref 29. In particular, we set $\tau_{112} = 10$ and $\tau_{110} = 5$. The numerical solution of the evolution problem is performed by a finite elements method exploiting the AMDiS toolbox.[42]

Photoluminescence Measurements. The optical properties of the NWs were probed using macro-PL measurements. The samples with as-grown wires were mounted in a vertically oriented helium flow cryostat with accurate temperature control. A 976 nm CW laser set to 41 mW, focused down to a spot of ∼35 μm in diameter using a using a 2.1 cm focal length off-axis parabolic mirror, was used for the excitation. The same mirror was then used to collimate the PL signal and couple it into a Thermo Scientific IS50r FTIR equipped with a liquid nitrogen cooled MCT detector. The thermal background radiation was minimized by modulating the laser at 35 kHz and using a lock-in amplifier, while operating the FTIR in step-scan mode. The full optical path was purged with nitrogen to minimize absorption due to water and carbon dioxide in air.

ASSOCIATED CONTENT

Supporting Information

The Supporting Information is available free of charge at https://pubs.acs.org/doi/10.1021/acsnano.9b09929.

Additional information on the surface energy calculations, incorporation energy, and shell growth model (PDF)

AUTHOR INFORMATION

Corresponding Authors

Simone Assali − *Department of Applied Physics, Eindhoven University of Technology, 5600 MB Eindhoven, The Netherlands; Department of Engineering Physics, École Polytechnique de Montréal, Montréal H3C 3A7, Canada;* orcid.org/0000-0002-3919-9112; Email: simone.assali@polymtl.ca

Roberto Bergamaschini − *L-NESS and Department of Materials Science, University of Milano Bicocca, 20125 Milano, Italy;* orcid.org/0000-0002-3686-2273; Email: roberto.bergamaschini@unimib.it

Emilio Scalise − *L-NESS and Department of Materials Science, University of Milano Bicocca, 20125 Milano, Italy;* orcid.org/0000-0003-1465-0939; Email: emilio.scalise@unimib.it

Authors

Marcel A. Verheijen − *Eurofins Materials Science BV, 5656AE Eindhoven, The Netherlands*

Marco Albani − *L-NESS and Department of Materials Science, University of Milano Bicocca, 20125 Milano, Italy;* orcid.org/0000-0002-8811-7574

Alain Dijkstra − *Department of Applied Physics, Eindhoven University of Technology, 5600 MB Eindhoven, The Netherlands;* orcid.org/0000-0003-2661-5460

Ang Li − *Department of Applied Physics, Eindhoven University of Technology, 5600 MB Eindhoven, The Netherlands; Beijing University of Technology, Beijing 100124, People's Republic of China*

Sebastian Koelling − *Department of Applied Physics, Eindhoven University of Technology, 5600 MB Eindhoven, The Netherlands;* orcid.org/0000-0002-6606-9110

Erik P. A. M. Bakkers − *Department of Applied Physics, Eindhoven University of Technology, 5600 MB Eindhoven, The Netherlands; Kavli Institute of Nanoscience, Delft University of Technology, 2600 GA Delft, The Netherlands;* orcid.org/0000-0002-8264-6862

Francesco Montalenti − *L-NESS and Department of Materials Science, University of Milano Bicocca, 20125 Milano, Italy;* orcid.org/0000-0001-7854-8269

Leo Miglio − *L-NESS and Department of Materials Science, University of Milano Bicocca, 20125 Milano, Italy;* orcid.org/0000-0002-1329-527X

Complete contact information is available at: https://pubs.acs.org/10.1021/acsnano.9b09929

https://dx.doi.org/10.1021/acsnano.9b09929
ACS Nano 2020, 14, 2445−2455

Author Contributions

¶S. Assali, R. Bergamaschini, and E. Scalise contributed equally to this work.

Notes

The authors declare no competing financial interest.

ACKNOWLEDGMENTS

The authors thank P. J. van Veldhoven for the technical support with the MOVPE reactor and L. Gagliano for the nanoimprint lithography of the Ge substrate. This work was supported by the Dutch Organization for Scientific Research (NWO-VICI 700.10.441) and by the Dutch Technology Foundation (STW 12744) and Philips Research. Solliance and the Dutch province of Noord-Brabant are acknowledged for funding the TEM facility. We acknowledge the CINECA award under the ISCRA initiative, for the availability of high-performance computing resources and support. A.D. acknowledges support from the NWO gravity program.

REFERENCES

(1) Soref, R. Mid-Infrared Photonics in Silicon and Germanium. *Nat. Photonics* **2010**, *4*, 495−497.

(2) Von Den Driesch, N.; Stange, D.; Wirths, S.; Mussler, G.; Holländer, B.; Ikonic, Z.; Hartmann, J. M.; Stoica, T.; Mantl, S.; Grützmacher, D.; Buca, D. Direct Bandgap Group IV Epitaxy on Si for Laser Applications. *Chem. Mater.* **2015**, *27*, 4693−4702.

(3) Aubin, J.; Hartmann, J. M.; Gassenq, A.; Rouviere, J. L.; Robin, E.; Delaye, V.; Cooper, D.; Mollard, N.; Reboud, V.; Calvo, V. Growth and Structural Properties of Step-Graded, High Sn Content GeSn Layers on Ge. *Semicond. Sci. Technol.* **2017**, *32*, No. 094006.

(4) Margetis, J.; Yu, S.-Q.; Bhargava, N.; Li, B.; Du, W.; Tolle, J. Strain Engineering in Epitaxial Ge1−xSnx: A Path towards Low-Defect and High Sn-Content Layers. *Semicond. Sci. Technol.* **2017**, *32*, 124006.

(5) Assali, S.; Nicolas, J.; Mukherjee, S.; Dijkstra, A.; Moutanabbir, O. Atomically Uniform Sn-Rich GeSn Semiconductors with 3.0−3.5 Mm Room-Temperature Optical Emission. *Appl. Phys. Lett.* **2018**, *112*, 251903.

(6) Attiaoui, A.; Moutanabbir, O. Indirect-to-Direct Band Gap Transition in Relaxed and Strained Ge1−x−ySixSny Ternary Alloys. *J. Appl. Phys.* **2014**, *116*, No. 063712.

(7) Assali, S.; Nicolas, J.; Moutanabbir, O. Enhanced Sn Incorporation in GeSn Epitaxial Semiconductors *via* Strain Relaxation. *J. Appl. Phys.* **2019**, *125*, No. 025304.

(8) Weisshaupt, D.; Jahandar, P.; Colston, G.; Allred, P.; Schulze, J.; Myronov, M. Impact of Sn Segregation on Ge1−xSnx Epi-Layers Growth by RP-CVD. In *2017 40th International Convention on Information and Communication Technology, Electronics and Microelectronics (MIPRO)*; IEEE, 2017; pp 43−47.

(9) Wirths, S.; Buca, D.; Mussler, G.; Tiedemann, A. T.; Hollander, B.; Bernardy, P.; Stoica, T.; Grutzmacher, D.; Mantl, S. Reduced Pressure CVD Growth of Ge and Ge1-XSnx Alloys. *ECS J. Solid State Sci. Technol.* **2013**, *2*, N99−N102.

(10) Biswas, S.; Doherty, J.; Saladukha, D.; Ramasse, Q.; Majumdar, D.; Upmanyu, M.; Singha, A.; Ochalski, T.; Morris, M. A.; Holmes, J. D. Non-Equilibrium Induction of Tin in Germanium: Towards Direct Bandgap Ge1−xSnx Nanowires. *Nat. Commun.* **2016**, *7*, 11405.

(11) Seifner, M. S.; Hernandez, S.; Bernardi, J.; Romano-Rodriguez, A.; Barth, S. Pushing the Composition Limit of Anisotropic Ge1-XSnx Nanostructures and Determination of Their Thermal Stability. *Chem. Mater.* **2017**, *29*, 9802−9813.

(12) Assali, S.; Dijkstra, A.; Li, A.; Koelling, S.; Verheijen, M. A.; Gagliano, L.; von den Driesch, N.; Buca, D.; Koenraad, P. M.; Haverkort, J. E. M.; Bakkers, E. P. A. M. Growth and Optical Properties of Direct Band Gap Ge/Ge0.87Sn0.13 Core/Shell Nanowire Arrays. *Nano Lett.* **2017**, *17*, 1538−1544.

(13) Meng, A. C.; Fenrich, C. S.; Braun, M. R.; McVittie, J. P.; Marshall, A. F.; Harris, J. S.; McIntyre, P. C. Core/Shell Germanium/Germanium-Tin Nanowires Exhibiting Room Temperature Direct- and Indirect-Gap Photoluminescence. *Nano Lett.* **2016**, *16*, 7521−7529.

(14) Seifner, M. S.; Dijkstra, A.; Bernardi, J.; Steiger-Thirsfeld, A.; Sistani, M.; Lugstein, A.; Haverkort, J. E. M.; Barth, S. Epitaxial Ge 0.81 Sn 0.19 Nanowires for Nanoscale Mid-Infrared Emitters. *ACS Nano* **2019**, *13*, 8047−8054.

(15) Doherty, J.; Biswas, S.; McNulty, D.; Downing, C.; Raha, S.; O'Regan, C.; Singha, A.; O'Dwyer, C.; Holmes, J. D. One-Step Fabrication of GeSn Branched Nanowires. *Chem. Mater.* **2019**, *31*, 4016−4024.

(16) Albani, M.; Assali, S.; Verheijen, M. A.; Koelling, S.; Bergamaschini, R.; Pezzoli, F.; Bakkers, E. P. A. M.; Miglio, L. Critical Strain for Sn Incorporation into Spontaneously Graded Ge/GeSn Core/Shell Nanowires. *Nanoscale* **2018**, *10*, 7250−7256.

(17) Assali, S.; Albani, M.; Bergamaschini, R.; Verheijen, M. A.; Li, A.; Kölling, S.; Gagliano, L.; Bakkers, E. P. A. M.; Miglio, L. Strain Engineering in Ge/GeSn Core/Shell Nanowires. *Appl. Phys. Lett.* **2019**, *115*, 113102.

(18) Gagliano, L.; Belabbes, A.; Albani, M.; Assali, S.; Verheijen, M. A.; Miglio, L.; Bechstedt, F.; Haverkort, J. E. M.; Bakkers, E. P. A. M. Pseudodirect to Direct Compositional Crossover in Wurtzite GaP/InxGa1−x P Core−Shell Nanowires. *Nano Lett.* **2016**, *16*, 7930−7936.

(19) Gagliano, L.; Albani, M.; Verheijen, M. A.; Bakkers, E. P. A. M.; Miglio, L. Twofold Origin of Strain-Induced Bending in Core−Shell Nanowires: The GaP/InGaP Case. *Nanotechnology* **2018**, *29*, 315703.

(20) Aubin, J.; Hartmann, J. M. GeSn Growth Kinetics in Reduced Pressure Chemical Vapor Deposition from Ge 2H6 and SnCl4. *J. Cryst. Growth* **2018**, *482*, 30−35.

(21) Margetis, J.; Yu, S.-Q.; Li, B.; Tolle, J. Chemistry and Kinetics Governing Hydride/Chloride Chemical Vapor Deposition of Epitaxial Ge1−x Sn X. *J. Vac. Sci. Technol., A* **2019**, *37*, No. 021508.

(22) Takeuchi, S.; Sakai, A.; Nakatsuka, O.; Ogawa, M.; Zaima, S. Tensile Strained Ge Layers on Strain-Relaxed Ge1−xSnx/Virtual Ge Substrates. *Thin Solid Films* **2008**, *517*, 159−162.

(23) Tsukamoto, T.; Hirose, N.; Kasamatsu, A.; Mimura, T.; Matsui, T.; Suda, Y. Investigation of Sn Surface Segregation during GeSn Epitaxial Growth by Auger Electron Spectroscopy and Energy Dispersive X-Ray Spectroscopy. *Appl. Phys. Lett.* **2015**, *106*, No. 052103.

(24) Groiss, H.; Glaser, M.; Schatzl, M.; Brehm, M.; Gerthsen, D.; Roth, D.; Bauer, P.; Schäffler, F. Free-Running Sn Precipitates: An Efficient Phase Separation Mechanism for Metastable Ge1−xSnx Epilayers. *Sci. Rep.* **2017**, *7*, 16114.

(25) Ragan, R.; Atwater, H. A. Diamond Cubic Sn-Rich Nanocrystals: Synthesis, Microstructure and Optical Properties. *Appl. Phys. A: Mater. Sci. Process.* **2005**, *80*, 1335−1338.

(26) Tran, R.; Xu, Z.; Radhakrishnan, B.; Winston, D.; Sun, W.; Persson, K. A.; Ong, S. P. Surface Energies of Elemental Crystals. *Sci. Data* **2016**, *3*, 160080.

(27) Cahn, J. W.; Taylor, J. E. Overview No. 113 Surface Motion by Surface Diffusion. *Acta Metall. Mater.* **1994**, *42*, 1045−1063.

(28) Albani, M.; Bergamaschini, R.; Salvalaglio, M.; Voigt, A.; Miglio, L.; Montalenti, F. Competition between Kinetics and Thermodynamics During the Growth of Faceted Crystal by Phase Field Modeling. *Phys. Status Solidi B* **2019**, *256*, 1800518.

(29) Salvalaglio, M.; Backofen, R.; Bergamaschini, R.; Montalenti, F.; Voigt, A. Faceting of Equilibrium and Metastable Nanostructures: A Phase-Field Model of Surface Diffusion Tackling Realistic Shapes. *Cryst. Growth Des.* **2015**, *15*, 2787−2794.

(30) Cahn, J. W.; Carter, W. C. Crystal Shapes and Phase Equilibria: A Common Mathematical Basis. *Metall. Mater. Trans. A* **1996**, *27*, 1431−1440.

(31) Tersoff, J. Kinetic Surface Segregation and the Evolution of Nanostructures. *Appl. Phys. Lett.* **2003**, *83*, 353−355.

(32) Bergamaschini, R.; Tersoff, J.; Tu, Y.; Zhang, J. J.; Bauer, G.; Montalenti, F. Anomalous Smoothing Preceding Island Formation During Growth on Patterned Substrates. *Phys. Rev. Lett.* **2012**, *109*, 156101.

(33) Meng, A. C.; Braun, M. R.; Wang, Y.; Fenrich, C. S.; Xue, M.; Diercks, D. R.; Gorman, B. P.; Richard, M.-I.; Marshall, A. F.; Cai, W.; Harris, J. S.; McIntyre, P. C. Coupling of Coherent Misfit Strain and Composition Distributions in Core-Shell Ge/Ge1-XSnx Nanowire Light Emitters. *Mater. Today Nano* **2019**, *5*, 100026.

(34) Stange, D.; Wirths, S.; Geiger, R.; Schulte-Braucks, C.; Marzban, B.; Den Driesch, N. V.; Mussler, G.; Zabel, T.; Stoica, T.; Hartmann, J.-M.; Mantl, S.; Ikonic, Z.; Grützmacher, D.; Sigg, H.; Witzens, J.; Buca, D. Optically Pumped GeSn Microdisk Lasers on Si. *ACS Photonics* **2016**, *3*, 1279−1285.

(35) Giannozzi, P.; Baroni, S.; Bonini, N.; Calandra, M.; Car, R.; Cavazzoni, C.; Ceresoli, D.; Chiarotti, G. L.; Cococcioni, M.; Dabo, I.; Dal Corso, A.; de Gironcoli, S.; Fabris, S.; Fratesi, G.; Gebauer, R.; Gerstmann, U.; Gougoussis, C.; Kokalj, A.; Lazzeri, M.; Martin-Samos, L.; Marzari, N.; et al. QUANTUM ESPRESSO: A Modular and Open-Source Software Project for Quantum Simulations of Materials. *J. Phys.: Condens. Matter* **2009**, *21*, 395502.

(36) Migas, D. B.; Borisenko, V. E.; Rusli; Soci, C. Revising Morphology of ⟨111⟩-Oriented Silicon and Germanium Nanowires. *Nano Convergence* **2015**, *2*, 16.

(37) Jain, A.; Ong, S. P.; Hautier, G.; Chen, W.; Richards, W. D.; Dacek, S.; Cholia, S.; Gunter, D.; Skinner, D.; Ceder, G.; Persson, K. A. Commentary: The Materials Project: A Materials Genome Approach to Accelerating Materials Innovation. *APL Mater.* **2013**, *1*, No. 011002.

(38) Grein, C. H. First Principles Calculations of Si(2 1 1) Surface Reconstructions. *J. Cryst. Growth* **1997**, *180*, 54−60.

(39) Backofen, R.; Bergamaschini, R.; Voigt, A. The Interplay of Morphological and Compositional Evolution in Crystal Growth: A Phase-Field Model. *Philos. Mag.* **2014**, *94*, 2162−2169.

(40) Backofen, R.; Rätz, A.; Voigt, A. Nucleation and Growth by a Phase Field Crystal (PFC) Model. *Philos. Mag. Lett.* **2007**, *87*, 813−820.

(41) Li, B.; Lowengrub, J. Geometric Evolution Laws for Thin Crystalline Films: Modeling and Numerics. *Commun. Comput.* **2009**, *6*, 433−482.

(42) Vey, S.; Voigt, A. AMDiS: Adaptive Multidimensional Simulations. *Comput. Visualization Sci.* **2007**, *10*, 57−67.

https://dx.doi.org/10.1021/acsnano.9b09929
ACS Nano 2020, 14, 2445−2455